Diagnosis of data assimilation systems by using normal modes

Nedjeljka Žagar

University of Ljubljana, Department of Physics
Jadranska 19, 1000 Ljubljana, Slovenia
nedjeljka.zagar@fmf.uni-lj.si

ABSTRACT

The application of the normal-mode functions to diagnose the atmospheric energy spectra in terms of balanced and inertio-gravity (IG) motions is presented. Results of the normal-mode diagnosis of the operational ECMWF analysis from July 2007 shows that roughly 10% of the wave (zonal wavenumber k≠0) motions is associated with IG waves and that the large-scale IG flow is confined to the tropics. It is illustrated how the normal-mode space can be used to intercompare the transient structure of large-scale waves in different analysis systems. Applied to both analysis and background fields the normal-mode expansion is used to diagnoze average and systematic analysis increments; the latter are interpreted as the analysis system bias.

1 Introduction

Normal modes are eigensolutions of the linearized primitive equations (Dickinson and Williamson 1972). The derivation of three-dimensional orthogonal normal-mode functions (NMFs) following Kasahara and Puri (1981) is provided in Appendix. Derived wave structures divide atmospheric motions into two kinds. The first kind consists of the eastward- and westward-propagating waves with high frequencies known as the inertio-gravity (IG) waves, denoted by EIG for eastward propagation and WIG for westward propagation. These motions can be represented predominantly by the velocity potential; therefore, they are essentially irrotational or divergent motions. In contrast, the second kind consists of the westward-propagating waves with low frequencies connected with the meridional variation of the horizontal component of the Coriolis vector. The second-kind of waves are represented essentially by the stream function, namely rotational, denoted by ROT; these waves are often referred to as the planetary waves similar to the Rossby-Haurwitz wave. The distinction between the ROT waves and the Rossby-Haurwitz wave is that, while the latter is purely non-divergent, the ROT waves include the large-scale effect of the divergence due to the curvature of spherical coordinates and the variation of latitude. Because the ROT waves are also quasi-geostrophic in nature, they are often referred to as a balanced mode in contrast to the IG waves which are ageostrophic and unbalanced.

In numerical weather prediction (NWP) models, normal modes have been used for the initialization purpose (e.g. Wergen 1988; Kleist et al. 2009). On large scales, the IG modes are most relevant in the tropics, as a significant part of the large-scale tropical variability is associated with the Kelvin, the mixed Rossby-gravity and other IG waves characterized by small phase speeds and equatorial trapping. Their diagnosis relies on mass-field information such as the outgoing longwave radiation (Wheeler and Kiladis 1999) and brightness temperature (Yang et al. 2003) or model outputs (e.g. Lin et al. 2006). On the contrary, by applying normal modes, the mass and wind fields of the waves are analyzed simultaneously. Since atmospheric motions are nonlinear, we cannot clearly separate them into the high-frequency IG and low-frequency ROT motions except in case of linearized equations around some specific background states. Nevertheless, the normal modes which are orthogonal and complete in functional representation and handle both the velocity and mass consistently are useful for analyzing the observed states of the real atmosphere, as shown by numerous studies.

The present application of the normal-mode expansion is performed with the purpose to estimate the contribution of IG motions to the 3D global flow in the ECMWF system, to analyze the balanced and IG enegry in terms different vertical and horizontal scales, and to diagnose some properties of the assimilation system by studying analysis increments. This paper extends results presented in Žagar et al. (2009a,b,c) and the reader is refered to these papers for details of methodology and further results.

2 The methodology of normal mode

The application of NMFs following Kasahara and Puri (1981) represents the three-dimensional global data vector $\left(u,v,g^{-1}P\right)^{\mathrm{T}}$ by the following finite series:

$$\left|\begin{array}{r} u(\lambda,\theta,\sigma) \\ v(\lambda,\theta,\sigma) \\ g^{-1}P(\lambda,\theta,\sigma) \end{array}\right| = \sum_{m=1}^{N_m} \mathbf{S}_m \left(\sum_{p=1}^{3} \sum_{n=0}^{N_n-1} \sum_{k=-N_k}^{N_k} \chi^p_{k,n,m} \mathbf{H}^p_{k,n,m}(\theta)\, e^{\mathrm{i}k\lambda} \right) \Pi_m(\sigma) \quad . \tag{1}$$

The data vector includes two wind components and the mass-field variable P, defined as $P = \Phi + RT_o\, ln(p_s)$. In this formula, $\Phi = gh$ is the geopotential, R is the gas constant, T_o is the globally average temperature on σ levels, g stands for gravity, while p_s is the surface pressure field.

The four-component index $\nu = (k,n,m,p)$ depends on the values of the zonal wavenumber k, meridional mode index n and vertical mode index m, in addition to the wave type, denoted by index p. Three values of p correspond to the EIG, WIG and ROT modes. The truncation indices N_m, N_k and N_n correspond, respectively, to the number of vertical modes, the number of waves along a latitude circle and a maximal number of meridional modes for a given (k,m,p) combination. Following Kasahara (1976), the mixed Rossby-gravity (MRG) mode is included as the $n = 0$ ROT mode (i.e., $\nu = (k,0,m,3)$) and the Kelvin mode is the $n = 0$ EIG wave (i.e., $\nu = (k,0,m,1)$). Other parameters are defined in the Appendix. The complex expansion coefficients χ_ν are non-dimensional. In order to represent the total energy in mode ν, $\chi_\nu(\chi_\nu)^*$ are multiplied by $(gH_{eq})^{1/2}$ which gives energy in units $\mathrm{m^2 s^{-2}}$ or $\mathrm{Jkg^{-1}}$.

The time-averaged analysis increment in mode ν is defined as

$$\overline{\Delta\chi_\nu} = \frac{1}{N_{smpl}} \sum_{t=1}^{N_{smpl}} \left[\chi^{an}_\nu(t) - \chi^{bg}_\nu(t) \right] \quad , \tag{2}$$

where the superscripts 'an' and 'bg' denote analysis and background fields, respectively. The parameter $\overline{\Delta E_\nu}$, defined as

$$\overline{\Delta E_\nu} = \sum_x g H_{eq,\nu} \overline{\left[\chi^{an}_\nu (\chi^{an}_\nu)^* - \chi^{bg}_\nu \left(\chi^{bg}_\nu\right)^* \right]} \quad , \tag{3}$$

can be used to represent the average tendency of the assimilation system to place or subtract the energy to/from a particular mode

Systematic analysis increments are indicative of the analysis system bias if they have amplitudes comparable to those of typical analysis increments (Dee 2005). This can be inspected by comparing Eq. (2) with the following equation which describes the energy distribution in increment fields at any analysis step:

$$E^{in}_\nu(t) = g H_{eq,\nu} \left[\left(\chi^{an}_\nu - \chi^{bg}_\nu\right) \left(\chi^{an}_\nu - \chi^{bg}_\nu\right)^* \right] \quad . \tag{4}$$

The distribution of time-averaged energy, $\overline{E^{in}_\nu(t)}$, shows parts of the modal space where the assimilation step on average makes most significant changes in the background.

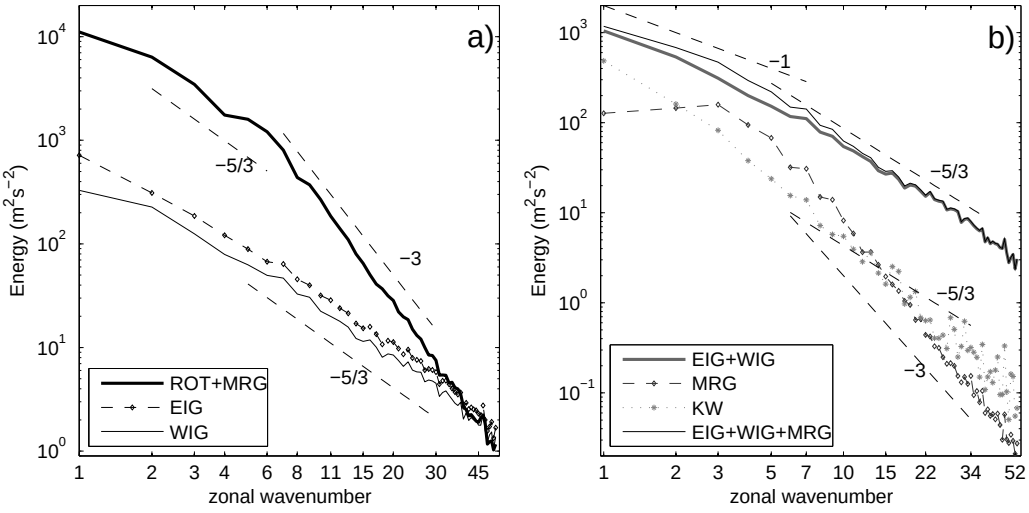

Figure 1: Total energy in balanced and inertio-gravity motions as a function of the zonal wavenumber obtained by averaging over 124 analyses for July 2007. Summation is performed over all (m,n).

3 Large-scale circulation in July 2007

The energy spectra separated into ROT and various IG components are presented in Fig. 1 as a function of the zonal wavenumber. In Fig. 1a, the MRG mode was included among the ROT modes while in Fig. 1b it is shown separately and its spectrum is added to that of IG motions as the MRG wave is usually considered the IG mode (e.g., Wheeler and Kiladis 1999). Thus the total IG motion is denoted IG+MRG. The zonally-averaged state ($k=0$) is not included in the plots as it contains an order of magnitude more energy than the wave motions ($k>0$). It can be seen that the balanced spectrum has the -3 slope over many scales smaller than the synoptic injection scale ($k=7-8$) whereas the slope of the IG motions across the same wavenumber range is close to $-5/3$. At the longest scales ($k=1-5$) the slope of the IG spectra is close to -1. The slope for the MRG wave appears flat for $k<5$ and it follows a -3 law at shorter scales; i.e. the MRG waves behave as balanced motions. The KW spectra show the same -3 slope except at the longest scales where the slope is close to $-5/3$, just like for the longest scales of the balanced motion. Figure 1 somewhat differs from the results for the ECMWF system in Žagar et al. (2009a) and Žagar et al. (2009b); the reason is the orography field which in the previous paper was retrieved from MARS as a surface field and did not exactly match model-level fields causing noisy spectra at smaller scales.

The relative contribution of IG motions to the total wave motion is around 10%. This is larger % than reported previously (Tanaka and Kimura 1996) but it agrees with laboratory experiments of Williams et al. (2008) and an increased level of IG energy in more recent analyses is expected given higher resolutions and improved model complexity in the tropics. There is more IG energy in EIG than in WIG motions and this is almost completely due to the Kelvin wave which is the most energetic IG motion.

Figure 2 presents circulations associated with balanced and IG modes averaged over the whole month for a single level in the upper and the lower troposphere. Notice that the length of wind vectors for balanced winds is three times smaller than for the IG flow. Nevertheless, it can be seen that the IG motions represent an important component of the large-scale flow in the tropics, especially over the Indian ocean and the Pacific. In agreement with a substantial role of the longest Kelvin waves in the tropics, a comparison of the lower and the upper troposphere in Fig. 2b,d can be used to argue about the validity of the classical 'first baroclinic mode' picture of the tropics applied in many simple models of the tropics (i.e., Gill 1980 and its follow-on studies). Figures 2b,d can be further split into contributions from various eastward- and westward-propagating modes as

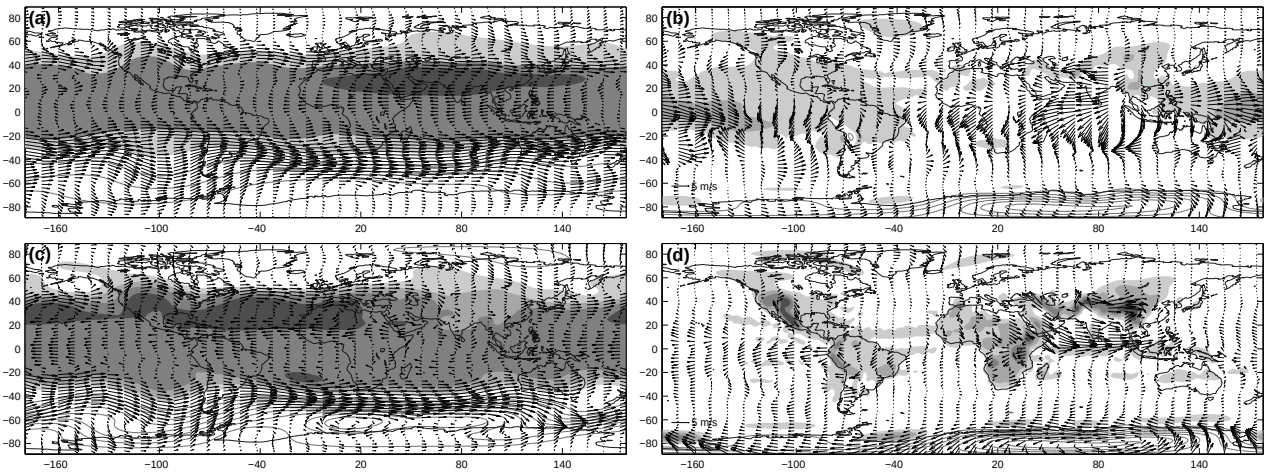

Figure 2: Average July 2007 (a,c) ROT+MRG and (b,d) IG circulations at a sigma level (a,b) 50 (∼212 hPa) and (c,d) 70 (∼671 hPa) according to the ECMWF analyses. Wind vectors in (a,c) have three times larger scaling factor than in (b,d). Positive values of the P variable are shaded and negative values are drawn by isolines. In (a,c) deviations from the global average of P are drawn with (a) positive contouring interval 150 m starting from +150 and negative contouring interval 300 m starting from −300 m, and in (c) contouring interval 50 m starting from ±50. In (b,d) the positive contouring interval is 20 m starting from +10 m while negative values are drawn every 50 m starting from −50 m.

illustarted in Žagar et al. (2009b).

In order to illustrate the potential of NMFs, we choose to present the temporal evolution of the MRG wave energy in three analysis datasets (Fig. 3) including the NCEP analyses and the NCEP/NCAR reanalyses in addition to ECMWF. The energy levels are very different in the three datasets because of differences in the analysis systems, especially the top model level. The NCEP/NCAR reanalysis system is produced at a lower horizontal resolution and the top model level is located at ∼2.7 hPa. The operational NCEP model was available on the T382 grid and its 64 vertical levels extend up to 32 Pa (around 60 km). On the other hand, the operational ECMWF model consists of 91 vertical levels up to 1 Pa (around 80 km) and horizontal T799 grid. It can be seen in Fig. 3 that, while the three solutions exhibit some similarity, there is a significant difference between the NCEP/NCAR and the other two datasets. Solutions nevertheless qualitatively agree about a number of episodes with increased energy in MRG motions: 15-16 July and 24 July in wavenumber $k = 2$, 1 July and 14 July in $k = 7$ and on 8-10 July in $k = 3$. Overall, the energy evolution appears rather similar in ECMWF and NCEP datasets with an active period between 4 and 18 July. In NCEP/NCAR the energy is concentrated at $k = 2$ most of time although the period from about 8 to 18 July is somewhat more energetic than the rest.

The average energy distribution in (m,k) space appears similar in NCEP and ECMWF (not shown); they both pick the zonal wave number $k = 3$ and the second vertical mode for the average energy maximum but the energy level is about 5 times greater in ECMWF than in NCEP analyses. While we do not have previous quantitative estimates to compare with, we notice that much of the difference between ECMWF and NCEP is accounted for by the MRG waves at the six upper-most levels in the ECMWF system which are located above 0.30 hPa.

An example of the difference between NCEP and ECMWF related to their vertical model depth is the event on 17 July in the ECMWF system (Fig. 3a). Its details can be studied by filtering back to grid-point space the wavenumber $k = 3$ at which the event appeared. The horizontal structure of the wave at model level 6 (∼0.28 hPa) at three subsequent times, shown in Fig. 4, illustrates the strengthening and westward propagation of the $k = 3$ wave over the Atlantic. The peak strength was at 12 UTC on 17 July, which was preceeded by a westward movement with speed around 18 m/s and amplitude growth. The westward propagation during the following 24 hours occurred at a nearly constant speed of 30 m/s with amplitude weakening. In the (m,t) space this

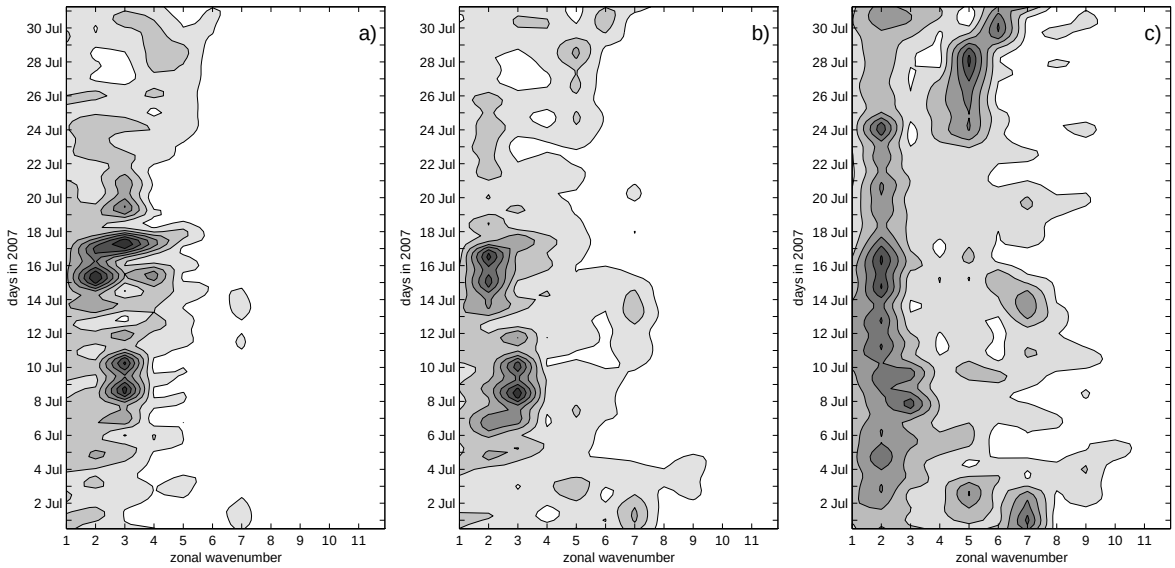

Figure 3: Evolution of the mixed Rossby-gravity wave energy in July 2007. (a) ECMWF, (b) NCEP and (c) NCEP/NCAR. Contouring levels are (in units of m^2/s^2): (a) every 60, starting from 60, (b) every 20, starting from 20 and (c) every 6, starting from 6. Ticks on the y-axis are drawn at 12 UTC on every other day.

event appears stationary which would imply very small vertical group velocity and therefore no vertical energy propagation. However, the short duration of the event and additional numerical damping at the top model levels makes an in-depth discussion of the event difficult.

4 Energy distibution of average and systematic analysis increments

Two-dimensional energy distibution of analysis increments defined by Eq. (4) is shown in Fig. 5 separately for ROT, EIG and WIG motions. Panels (a-c), which show the (n,m) distribution, can be compared with Fig. 7 (panels d-f) in Žagar et al. (2009a) showing the energy distribution of full fields. The comparison shows that the largest changes are made in the most energetic part of the wave flow for all three motion types. The maximal ROT energy in $(n,m) = (1-2,2)$ in Fig. 5a corresponds to large increments made at the model top levels. The secondary maximum centered at $(n,m) = (4,6)$ which corresponds to the levels lower in the stratosphere and in the upper troposphere. About 60% of the total increment wave energy is in the ROT modes, the rest is about equally divided between the EIG and WIG modes. The zonally averaged state is not included in the summation shown in the two figures. Adding $k = 0$ would changes panels (a-c) by incresing energy amounts in $n = 1-3$ across a range of leading m in both EIG and WIG motions (figures not shown). Around 30% of the total increment energy is in the $k = 0$ state but the relative contribution of balanced and IG modes remains about the same. On the contrary, the $k = 0$ state in full fields is predominantly balanced (Žagar et al. 2009a).

The (n,k) distribution (Fig. 5d-f) can be compared with the (n,k) energy distribution of time-averaged analysis increments, defined by Eq. (3), used as an indication of the analysis system bias (Fig. 6). For the WIG and EIG modes, two distributions appear rather similar, especially in the appearance of the maximum in $(n,k) = (2,0)$. The negative $k = 1$ Kelvin wave bias suggests that overall the assimilation system in July 2007 tended to supress the Kelvin wave (Fig. 6b). Positive biases in ROT modes are largest in $(n,k) = (1-2,2)$ which corresponds to $m = 2$ i.e., the top model levels as discussed in Žagar et al. (2009). The comparable amplitudes in Fig. 5 and Fig. 6 associated with the leading vertical modes and longest zonal scales are due to difficulties with the treatment of mesospheric levels in the model and assimilation. This is further illustrated in Fig. 7 which

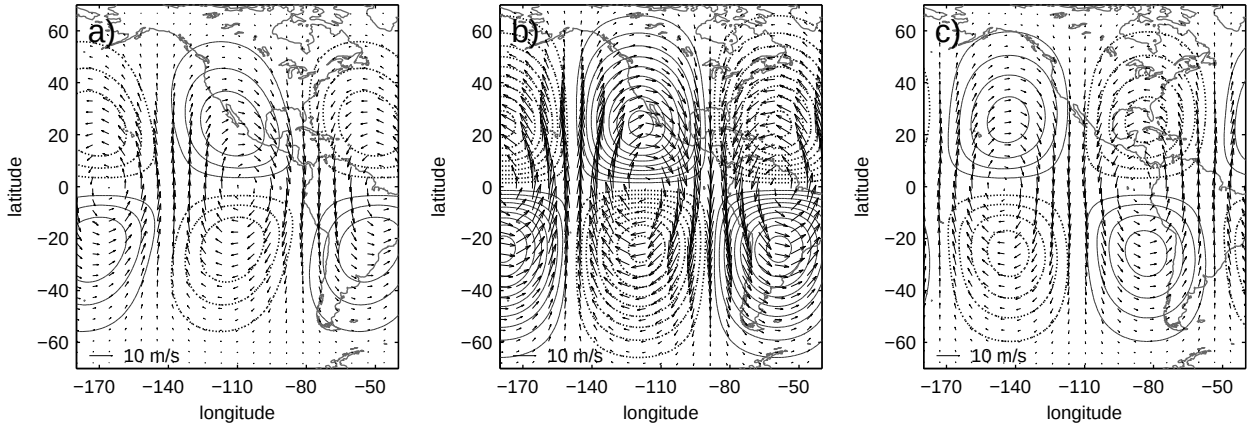

Figure 4: Horizontal structure of the $k = 3$ mixed Rossby-gravity wave in the ECMWF analyses at model level 6 ($\sim$ 0.28 hPa). (a) 17 July, 00 UTC, (b) 17 July, 12 UTC, (c) 18 July, 12 UTC. P isolines are drawn every $\pm$10 m, starting from $\pm$10 m and the zero isoline is omitted.

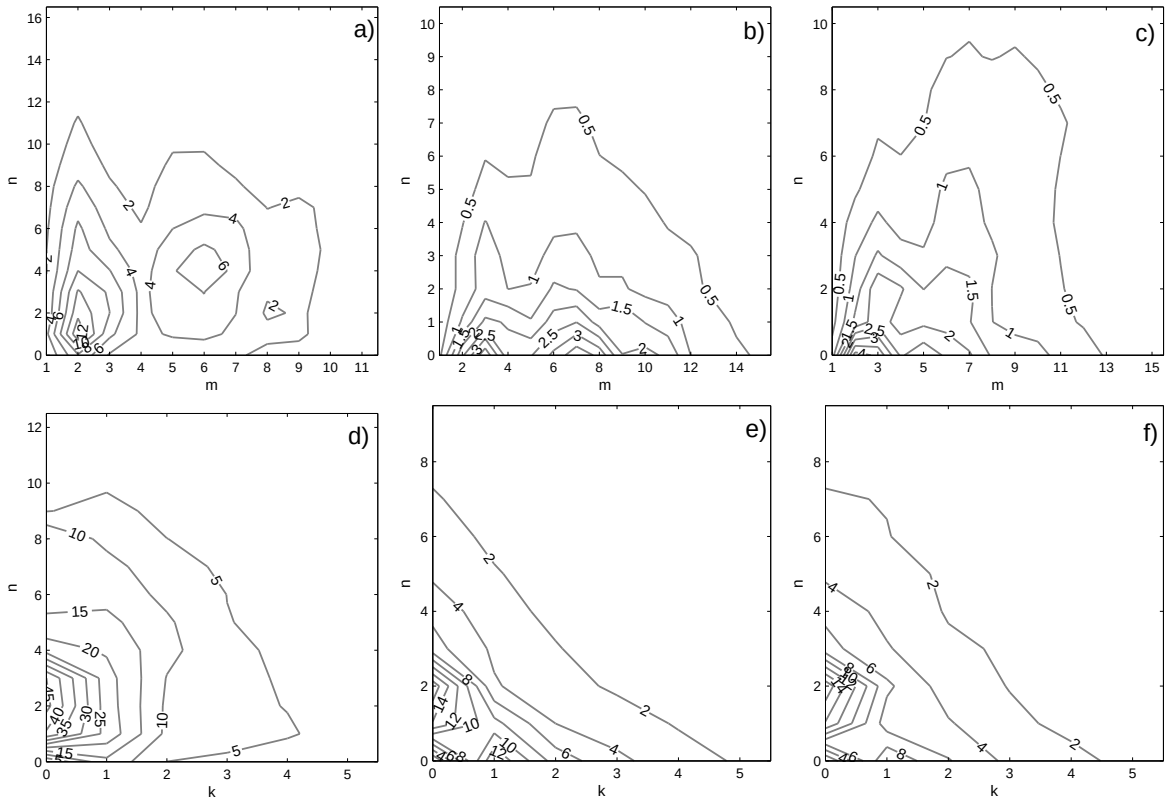

Figure 5: Average energy of analysis increments (in m^2s^{-2}) in July 2007. (a,d) ROT+MRG modes, (b,e) EIG modes, (c,f) WIG modes. $k = 0$ is not included in the summation in (a-c).

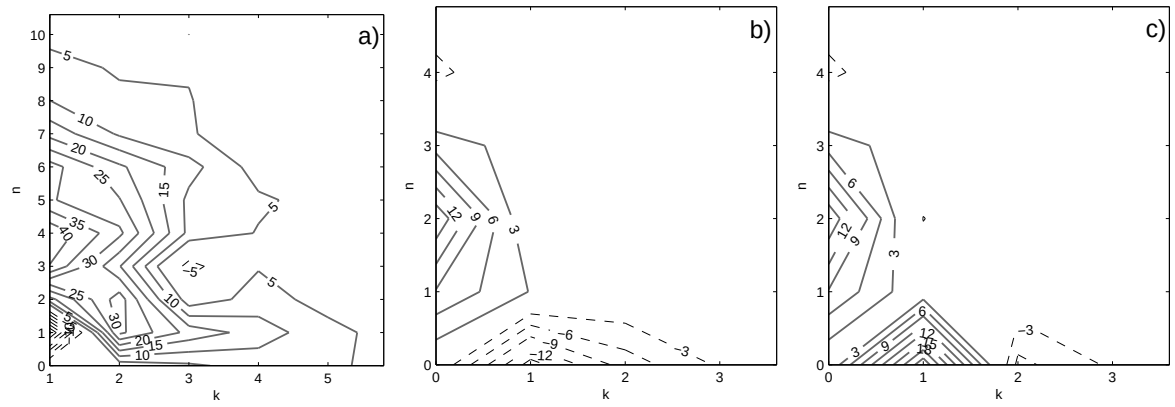

Figure 6: The (k,n) distribution of $\overline{\Delta E_v}$ (in $m^2 s^{-2}$) in July 2007. Summation is perfomed over all m. (a) ROT+MRG modes, (b) EIG modes, (c) WIG modes.

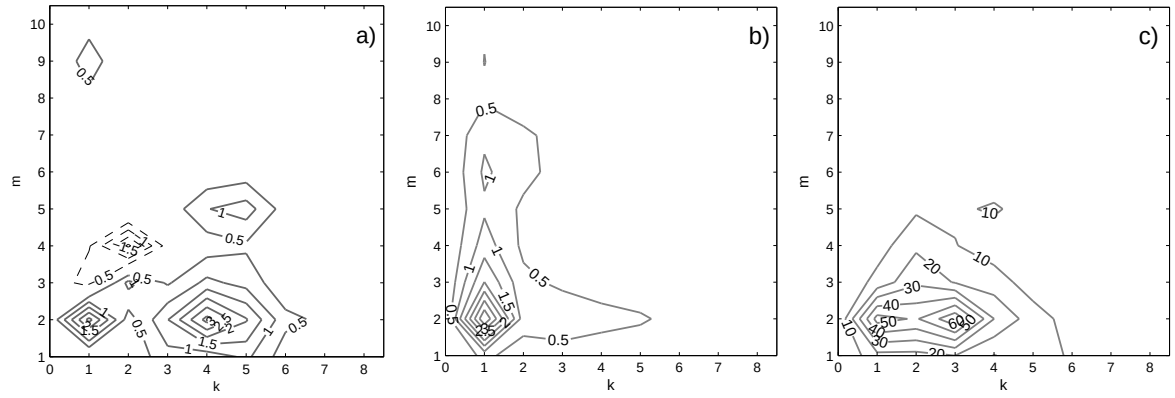

Figure 7: (a) As in Fig. 6 but the MRG wave. (b) As in Fig. 5 but the MRG wave. (c) Average energy distribution for the MRG mode in full dynamical fields.

compares the bias in the MRG mode with its average increment and energy in this mode in full fields.

5 Concluding remark

Presented application of the normal-mode function expansion shows that their usefulness in the NWP framework extends beyond that of the non-linear normal-mode initialization. Normal modes can be a useful tool for the identification of the analysis system bias and for understanding of the balance issues of relevance for data assimilation.

APPENDIX

Normal modes of Kasahara and Puri (1981)

The derivation of normal modes starts from the primitive equations with the traditional shallowness approximations written in σ coordinates. The equations are linearized around a motionless mean state with a vertical temperature profile T_o as a function of σ. By introducing a new mass variable P, as defined in section 2, the thermodynamic and continuity equations can be combined into a single equation for the P variable.

Solutions to the adiabatic and inviscid linearized equations are sought by assuming separability of the vertical and horizontal dependences of the dependent variables. Introducing the vertical dependence function $\Psi(\sigma)$, the zonal and the meridional wind (u and v respectively) and the geopotential variable P are expressed by

$$\begin{vmatrix} u(\lambda,\theta,\sigma) \\ v(\lambda,\theta,\sigma) \\ g^{-1}P(\lambda,\theta,\sigma) \end{vmatrix} = \begin{vmatrix} u'(\lambda,\theta) \\ v'(\lambda,\theta) \\ g^{-1}P'(\lambda,\theta) \end{vmatrix} \Psi(\sigma)\,. \tag{A-1}$$

Substituting (A-1) into the linearized equations leads to the two standard systems of horizontal and vertical structure equations. The system of equations for horizontal motions for u', v' and h' on the sphere are written after dropping the prime symbols as follows:

$$\frac{\partial u}{\partial t} - 2\Omega\mu v + \frac{g}{a}\left(1-\mu^2\right)^{-1/2}\frac{\partial h}{\partial \lambda} = 0 \tag{A-2}$$

$$\frac{\partial v}{\partial t} + 2\Omega\mu u + \frac{g}{a}\left(1-\mu^2\right)^{1/2}\frac{\partial h}{\partial \mu} = 0 \tag{A-3}$$

$$\frac{\partial h}{\partial t} + \frac{H_{eq}}{a}\left[\frac{\partial u}{\partial \lambda} + \frac{\partial}{\partial \mu}\left(\left(1-\mu^2\right)^{1/2} v\right)\right] = 0\,. \tag{A-4}$$

All constants here are represented by their usual symbols: t stands for time, $\mu = sin(\theta)$, a is the radius of the earth and Ω is the earth's rotation speed. A constant H_{eq}, which has the dimension of length, couples the horizontal Eqs. (A-2-A-4) and the following vertical structure equation:

$$\frac{d}{d\sigma}\left(\frac{\sigma g}{R\Gamma_o}\frac{d\Psi}{d\sigma}\right) + \frac{1}{H_{eq}}\Psi = 0\,. \tag{A-5}$$

The constant H_{eq} is thus the eigenvalue of Eq. (A-5). A subscript '*eq*' stands for the '*equivalent depth*' as this parameter is best known; this comes from the equivalency of Eq. (A-2-A-4) to linearized shallow-water equations with the fluid depth of H_{eq}.

The solutions of the vertical structure equation require two boundary conditions, at the model top and bottom half levels ($\sigma = 0$ and $\sigma = 1$ respectively):

$$\frac{d\Psi}{d\sigma} = \text{finite at } \sigma = 0, \quad \text{and} \quad \frac{d\Psi}{d\sigma} + \frac{\Gamma_o}{T_o}\Psi = 0 \text{ at } \sigma = 1\,. \tag{A-6}$$

In addition to the vertical discretization in terms of σ levels, Eq. (A-5) requires as input the vertical stability profile Γ_o, defined as

$$\Gamma_o = \frac{\kappa T_o}{\sigma} - \frac{dT_o}{d\sigma}\,. \tag{A-7}$$

The parameter κ is defined as $\kappa = R/C_p$ where C_p is the specific heat at constant pressure. The spectrum of solutions of (A-5) is discrete and it is given in terms of vertical eigenfunctions $\Pi_m(\sigma)$, where m ranges between 1 and N_σ, the number of vertical levels.

Solutions of the system (A-2-A-4) are given in terms of Hough functions (Kasahara 1976; Kasahara 1978):

$$(u,v,h)^{\mathrm{T}} = \mathbf{S}_m \mathbf{H}^p_{k,n}(\lambda,\theta,m)\, e^{-\mathrm{i}\,\omega_{k,n,m} p t}\,, \tag{A-8}$$

where $\omega_{k,n,m}$ is the eigenfrequency. Also, $\mathbf{S}_m$ represents the scaling matrix which removes dimensions from the input data vector after the vertical projection is performed:

$$\mathbf{S}_{\mathrm{m}} = \begin{pmatrix} (gH_{eq})^{1/2} & 0 & 0 \\ 0 & (gH_{eq})^{1/2} & 0 \\ 0 & 0 & H_{eq} \end{pmatrix}. \tag{A-9}$$

The symbol $\mathbf{H}^p_{k,n}(\lambda,\theta,m)$ represents the Hough harmonics, which are built as:

$$\mathbf{H}^p_{k,n}(\lambda,\theta,m) = \mathbf{H}^p_{k,n}(\theta,m)\, e^{-\mathrm{i}k\lambda}\,. \tag{A-10}$$

The zonal part is given in terms of harmonic waves while the meridional part, the Hough function $\mathbf{H}^p_{k,n}$, is a vector function of latitude for each vertical mode m and motion type p:

$$\mathbf{H}^p_{k,n} \equiv \begin{bmatrix} U^p_{k,n,m}(\theta) \\ -\mathrm{i}V^p_{k,n,m}(\theta) \\ Z^p_{k,n,m}(\theta) \end{bmatrix} \tag{A-11}$$

The meridional structure functions $U^p_{k,n,m}$, $V^p_{k,n,m}$ and $Z^p_{k,n,m}$ were derived by Kasahara (1976) for $k \neq 0$ and the case $k = 0$ is treated in Kasahara (1978).

References

Dee, D. P., 2005: Bias and data assimilation. *Q. J. R. Meteorol. Soc.* **131**, 3323–3343.

Dickinson, R. E. and D. L. Williamson, 1972: Free oscilations of a descrete stratified fluid with application to numerical weather prediction. *J. Atmos. Sci.* **29**, 623–640.

Gill, A. E., 1980: Some simple solution for heat-induced tropical circulation. *Q. J. R. Meteorol. Soc.* **106**, 447–462.

Kasahara, A., 1976: Normal modes of ultralong waves in the atmosphere. *Mon. Wea. Rev.* **104**, 669–690.

Kasahara, A., 1978: Further studies on a spectral model of the global barotropic primitve equations with hough harmonic expansions. *J. Atmos. Sci.* **35**, 2043–2051.

Kasahara, A. and K. Puri, 1981: Spectral representation of three-dimensional global data by expansion in normal mode functions. *Mon. Wea. Rev.* **109**, 37–51.

Kleist, D. T., D. F. Parrish, J. C. Derber, R. Treadon, R. M. Errico, and R. Yang, 2009: Improving incremental balance in the GSI 3DVAR analysis system. *Mon. Wea. Rev.* **137**, 1046–1060.

Lin, J.-L., G. Kiladis, B. E. Mapes, K. M. Weickmann, K. R. Sperber, W. Lin, M. C. Wheeler, S. D. Schubert, A. D. Genio, L. J. Donner, S. Emori, J.-F. Gueremy, F. Hourdin, P. J. Rasch, E. Roeckner, and J. F. Scinocca, 2006: Tropical Intraseasonal Variability in 14 IPCC AR4 Climate Models. Part I: Convective Signals. *J. Climate* **19**, 2665–2690.

Tanaka, H. and K. Kimura, 1996: Normal-mode energetics analysis and the intercomparison for the recent ECMWF, NMC, and JMA global analyses. *J. Meteor. Soc. Japan* **74**, 525–538.

Žagar, N., J. Tribbia, J. L. Anderson, and K. Raeder, 2009a: Uncertainties of estimates of inertio-gravity energy in the atmosphere. Part I: intercomparison of four analysis datasets. *Mon. Wea. Rev.* **137**, in print.

Žagar, N., J. Tribbia, J. L. Anderson, and K. Raeder, 2009b: Uncertainties of estimates of inertio-gravity energy in the atmosphere. Part II: large-scale equatorial waves. *Mon. Wea. Rev.* **137**, in print.

Žagar, N., J. Tribbia, J. L. Anderson, K. Raeder, and D. T. Kleist, 2009: Diagnosis of systematic analysis increments by using normal modes. *Q. J. R. Meteorol. Soc.* **135**, submitted.

Wergen, W., 1988: The diabatic ECMWF normal mode initialization scheme. *Beitr. Phys. Atmosph.* **61**, 274–302.

Wheeler, M. and G. N. Kiladis, 1999: Convectively coupled equatorial waves: analysis of clouds and temperature in the wavenumber-frequency domain. *J. Atmos. Sci.* **56**, 374–399.

Williams, P. D., T. W. N. Haine, and P. L. Read, 2008: Inertia-gravity waves emitted from balanced flow: Observations, properties, and consequences. *J. Atmos. Sci.* **65**, 3543–3556.

Yang, G.-Y., B. J. Hoskins, and J. Slingo, 2003: Convectively coupled equatorial waves: A new methodology for identifying wave structures in observational data. *J. Atmos. Sci.* **60**, 1637–1654.